RSC Advances

ROYAL SOCIETY OF CHEMISTRY

PAPER

View Article Online
View Journal | View Issue

Check for updates

Cite this: *RSC Adv.*, 2025, **15**, 33830

Significance of the direct relation between the fill factor and hole transport layer thickness in perovskite-based solar cells for green energies

Muhammad Mubeen Mudassar,[a] Mehwish Arshad,[a] Muhammad Umar Salman,[a] Asif Mahmood,[b] Waheed Al-Masry,[b] Muhammad Asim[c] and Shahid Atiq*[a]

Received 27th August 2025
Accepted 31st August 2025

DOI: 10.1039/d5ra06410d

rsc.li/rsc-advances

In response to the growing global energy crisis and environmental degradation, the development of clean, sustainable energy technologies is imperative. Solar energy, with its vast availability and minimal ecological footprint, is a leading candidate. Among the emerging photovoltaic technologies, perovskite solar cells (PSCs) are gaining attention for their tuneable optoelectronic properties and low-cost processing. This study employs a 2D model simulation on COMSOL Multiphysics to investigate two lead-free PSC designs, focusing on structural optimization. Notable results for the ZnSe/$BiFeO_3$/spiro-OMeTAD cell include a maximum short-circuit current density (J_{sc}) of 9.83 mA cm^{-2} and a peak efficiency of 10.72% at 75 nm electron transport layer thickness, open-circuit voltage (V_{oc}) of 2.2 V at 125 nm hole transport layer thickness, and fill factor (FF) of 73.77% at 100 nm BFO thickness. For the ZnSe/$CsSnI_3$/spiro cell, a maximum efficiency of 17.56%, FF of 79.91%, V_{oc} of 1.01 V, and J_{sc} of 28.32 mA cm^{-2} were achieved. The study specifically explored the direct relation between the FF and hole transport layer thickness in a perovskite-based green photovoltaic device. These findings highlight the promising potential of lead-free perovskites for efficient, stable, and environmentally benign solar cells. This work supports the advancement of inorganic PSCs, contributing to the global shift toward renewable energy.

1. Introduction

Global energy demand continues to rise steadily, driven by rapid population growth, which is projected to reach 10 billion by 2050, along with an increasing dependence on energy-intensive technologies, resulting in annual energy consumption that is expected to increase by nearly 1.7%.[1–3] To meet this growing demand, around 30 terawatts (TW) of energy will be required by 2050.[4] Despite this need, energy production still heavily relies on non-renewable fossil fuels such as petroleum, coal, and natural gas, which take millions of years to replenish.[5] The combustion of these fuels releases greenhouse gases and toxic pollutants, contributing to ozone depletion and climate change.[6,7] In 2017 alone, approximately 19 billion tons of toxic gases (*e.g.* carbon monoxide) were released into the atmosphere, accounting for 53% of global emissions.[8] To address these environmental concerns, the energy sector is shifting toward renewable sources, such as solar and wind, which offer environmental and economic advantages, as well as sustainability.[9,10] Among these technologies, solar energy is particularly promising due to its abundance and accessibility. Photovoltaic (PV) technology plays a central role by converting sunlight directly into electricity through the PV effect.[10–12] Perovskite solar cells (PSCs) have emerged as a leading PV technology due to their tuneable bandgap, long carrier lifetime, and extended diffusion lengths. These features have enabled a rapid increase in power conversion efficiency (PCE), rising from 3.8% in 2009 to ∼27% at present, competing with the performance of conventional silicon-based solar cells.[13–17] The basic structure of PSCs consists of three functional layers: the electron transport layer (ETL); the perovskite (PVK) or absorber layer, which generates charge carriers; and the hole transport layer (HTL), which extracts holes from the absorber and transfers them to the back electrode.

In PSCs, the ETL is a crucial component that enables efficient charge extraction while minimizing recombination losses by maximizing electron transfer from the absorber layer to the front electrode. Zinc selenide (ZnSe) is widely employed as an ETL in PSCs due to its exceptional properties, including a bandgap of approximately ∼2.6–3.1 eV, non-toxic nature, cost-effectiveness, and excellent optical transparency in the visible spectrum.[4,18–21] This absorber layer, composed of PVK material with exceptional optoelectronic properties, serves as the most vital part of PSCs, efficiently capturing incident light and generating charge carriers.[22] The PVK material generally follows the ABX_3 crystalline formula, where 'A' represents an

---

[a] *Centre of Excellence in Solid State Physics, University of the Punjab, Lahore 54590, Pakistan. E-mail: satiq.cssp@pu.edu.pk*
[b] *College of Engineering, Chemical Engineering Department, King Saud University, Riyadh, 11421, Saudi Arabia*
[c] *Department of Physics and Astronomy, Sejong University, Seoul, South Korea*

electropositive cation, 'B' denotes a magnetic cation (*e.g.*, Fe), and 'X' corresponds to oxygen anions. The lead-free multiferroic BFO was utilized as an absorber layer, which exhibited a direct bandgap ranging from 2.1–2.7 eV and an indirect bandgap of approximately 1.07 eV, making it highly suitable for PV applications due to its bandgap tunability within the visible spectrum while adopting a rhombohedral crystal symmetry and belonging to the *R*3*c* space group.[1,23] At room temperature, the BFO material exhibits both antiferromagnetic (Néel temperature ∼ 643 K) and ferroelectric ordering (Curie temperature ∼ 1103 K).[24,25] Complementing BFO, the $CsSnI_3$ perovskite serves as an efficient absorber with a direct bandgap near 1.3 eV, enabling strong absorption in the visible spectrum.[26–28] It crystallizes in an orthorhombic phase at room temperature, which supports excellent charge carrier mobility and strong light-harvesting capability.[29] The material's intrinsic properties facilitate efficient electron–hole generation, making $CsSnI_3$ a promising absorber layer for lead-free, environmentally friendly solar cells. Spiro-OMeTAD is widely recognized as a high-performance HTL due to its high hole mobility, large bandgap (3 eV), low electron mobility, exceptional film formation, relatively low electron affinity (1.9 eV), and high stability with the absorber layer.[7,22,30–32]

In recent studies, Rahmoune *et al.* (2023) reported a PCE of approximately ∼28% for the $ZnSe/MoS_2/Sb_2S_3$ configuration, as simulated using the SCAPS-1D framework.[22] Using the same software, Kumar *et al.* (2024) demonstrated a fill factor (FF) of around 29.10% utilizing BFO as the absorber layer and ZnO as the ETL.[33] Complementarily, Salman *et al.* (2025) employed COMSOL Multiphysics simulations to explore a ZnO/BFO-based device architecture incorporating spiro-OMeTAD as the HTL, achieving a notable PCE of 11.92%.[26] Moreover, Raj *et al.* (2024) investigated a lead-free PSC configuration comprising FTO/TiO_2/BFO/spiro-OMeTAD/Au and attained a remarkable efficiency of 5.06%.[1] Interestingly, an HTL-free PSC structure using BFO as the absorber layer demonstrated an impressive PCE of 11.92% for the FTO/ZnO/BFO device configuration, as reported by Sahoo *et al.* (2024).[23] In addition, Ameen *et al.* (2025) revealed a notable PCE of ∼11.79% by employing BFO as the main layer and ZnO as an ETL within a 1D solar cell model simulated using the COMSOL Multiphysics tool.[34]

A comprehensive review of the existing literature indicates that extensive simulation studies employing SCAPS-1D have been conducted on ZnSe, BFO, and spiro-OMeTAD. However, no specific research has been undertaken on the 2D ZnSe/BFO/spiro-OMeTAD configuration of PSCs; therefore, this study focuses on simulating its 2D architecture by using the COMSOL Multiphysics software. This computational tool employs the finite element method (FEM) for solving complex modules, with the added advantage of incorporating multi-physics domains by selecting appropriate models.[35] The study aims to optimize key parameters such as layer thickness and acceptor and donor densities (N_A/N_D) to achieve improved PCE while systematically analysing and evaluating the direct relation between FF and HTL thickness for green energy.

2. Numerical modelling

COMSOL Multiphysics is a simulation software used to study how different physical processes work together in real-world devices. In solar cell research, it helps model how light is absorbed, how electric charge moves, and how energy is converted into electricity. The software solves mathematical equations that describe these processes, allowing researchers to test different materials, layer thicknesses, and device designs without making physical prototypes. This makes it easier to understand and improve the performance of solar cells using accurate, computer-based experiments. In this study, we will use COMSOL to solve Poisson's equation, current density equations, continuity equations, and the Shockley–Read–Hall recombination model to analyze the charge transport and recombination mechanisms inside the solar cell.[36] Poisson's equation (eqn (1)) tells us how the electric potential is distributed inside a device due to the presence of electric charges. It helps in determining the internal electric field (E) that drives charge carrier movement in a solar cell:[37,38]

$$\frac{\partial^2 \psi}{\partial x^2} = -\frac{\partial E}{\partial x} = -\frac{\rho}{\varepsilon_s} = -\frac{q}{\varepsilon_s}[p - n + N_D{}^+(x) - N_A{}^-(x) \pm N_t(x)] \tag{1}$$

Here, in eqn (1), ψ is the electrostatic potential and ρ is the total charge density influenced by free charge carriers (p, n), ionized dopants ($N_D{}^+$, $N_A{}^-$), and trap charge density (N_t). The parameters ε_s and q represent the semiconductor's permittivity and elementary charge, respectively. The continuity equations (eqn (2) and (3)) describe how the number of charge carriers changes over time due to generation, recombination, and flow. It ensures charge conservation within the semiconductor device:[39,40]

$$-\frac{\partial J_p}{\partial x} + G - U_p(n,p) = 0 \tag{2}$$

$$\frac{\partial J_n}{\partial x} + G - U_n(n,p) = 0 \tag{3}$$

In eqn (2) and (3), J_p and J_n represent the electron and hole current densities, while G is the generation rate, and $U_p(n, p)$, $U_n(n, p)$ are the respective recombination rates. These equations (eqn (2) and (3)) ensure that carrier generation, recombination, and flow are balanced at every point in the device. The current density equations, given as eqn (4) and (5), describe how electrons and holes move through the device due to the electric field and concentration gradient:[39,40]

$$J_p = qn\mu_p E - qD_p \frac{\partial p}{\partial x} J_p \tag{4}$$

$$J_n = qn\mu_n E - qD_n \frac{\partial p}{\partial x} J_n \tag{5}$$

Here, in eqn (4) and (5), J_n and J_p represent the total electron and hole current densities, combining drift due to the electric field E, and diffusion caused by carrier concentration gradients. The terms q, μ, and D indicate the charge, mobility, and diffusion coefficients that control the carrier transport in the solar cell. Here, μ refers to the ability of charge carriers to move through a semiconductor under the influence of an electric field, and it directly determines how efficiently electrons and holes can be transported toward their respective electrodes. The SRH recombination equation (eqn (6)) explains how charge carriers recombine through defect states in the bandgap, reducing carrier lifetime. It depends on electron and hole concentrations, intrinsic carrier density, and their respective lifetimes:

$$R_{\mathrm{SRH}} = \frac{np - \gamma_{\mathrm{n}}\gamma_{\mathrm{p}}{n_{\mathrm{i}}}^2}{\tau_{\mathrm{n}}(p + p_i) + \tau_{\mathrm{p}}(n + n_{\mathrm{i}})} \tag{6}$$

in eqn (6), R_{SRH} represents the recombination rate through defect states, depending on carrier concentrations, n_{i} represents the intrinsic carrier density. The terms γ_{n}, γ_{p}, and p_{i} adjust the recombination rate based on material-specific trap characteristics.[41,42] The lifetime equation, given in eqn (7), indicates the average time a charge carrier survives before recombining, and it is a key parameter for assessing recombination losses and overall device performance:[43]

$$\tau = \frac{1}{\sigma \times N_{\mathrm{t}} \times \nu_{\mathrm{th}}} \tag{7}$$

Here, in eqn (7), τ represents the carrier lifetime, which depends on the trap density N_{t}, capture cross-section (σ), and thermal velocity is denoted by ν_{th}. N_{t} refers to the concentration of defect states within the bandgap of the semiconductor that can capture and release charge carriers, thereby strongly influencing recombination dynamics and overall device performance. It indicates how quickly carriers are captured by traps and recombine, affecting device performance. This study uses COMSOL Multiphysics to simulate the internal behaviour of a solar cell by modelling charge movement, generation, and loss mechanisms. It helps visualize how carriers behave within the device and how different physical parameters affect performance. Through this numerical approach, the efficiency and reliability of the solar cell can be accurately analysed and optimized.

SCAPS-1D is a widely used, dedicated solar cell simulation tool that solves the coupled drift-diffusion, Poisson, and continuity equations in a 1-dimensional framework. It is highly efficient for the layer-by-layer analysis of carrier transport, defect states, and recombination dynamics, and has become a standard in perovskite and thin-film device modelling. However, its scope is mainly limited to 1D device geometries, and it doesn't easily extend to complex multi-dimensional effects such as lateral inhomogeneities, textured interfaces, or optical field distribution in 2D/3D space.[44,45] On the other hand, COMSOL Multiphysics is a finite element method-based platform that allows the simultaneous coupling of electrical, optical, and thermal physics in arbitrary geometries. For our study, COMSOL was particularly advantageous because it not only captured the electronic transport in BFO-based devices, but also allowed us to incorporate optical absorption profiles and band alignment at the interfaces in a spatially resolved manner. Moreover, COMSOL can handle multi-physics coupling (*e.g.*, piezoelectric and ferroelectric effects, if needed for multiferroic absorbers), which is critical for exploring the intrinsic photovoltaic potential of BFO, something that SCAPS cannot directly address.

3. Device simulation and methodology

3.1 Solar irradiance patterns for optimized energy harvesting

Fig. 1(a) presents the solar spectrum across a broad range of wavelengths and illustrates the absorption spectra of various PV technologies in solar cell research. The solar irradiance ranges from 1 to approximately 1.6 W m^{-2} nm^{-1}, corresponding to a wavelength range of 300 nm to 2500 nm. Solar radiation is distributed across spectral regions according to wavelength, and the spectrum that reaches the earth's surface is influenced by atmospheric absorption, such as by ozone, water vapor, and oxygen molecules. The peak solar irradiance occurs near 460 nm; beyond this peak, irradiance gradually decreases for two primary reasons: (1) longer wavelengths carry lower photon energy ($E = hc/\lambda$), making them less effective at exciting electrons; (2) stronger absorption of infrared radiation by atmospheric water vapor reduces the intensity. At ground level, the solar spectrum can be categorized into three regions: approximately 5% of the irradiance falls in the ultraviolet (UV) range (300–400 nm), around 43% lies in the visible spectrum (400–700 nm), and about 52% is contained in the infrared (IR) region (700–2500 nm). The visible spectrum contributes most significantly to absorption in solar cells, resulting in efficient charge carrier generation. The PCE is conventionally evaluated under AM 1.5 conditions, which represent realistic sunlight exposure. The AM 1.5 spectrum is also crucial in guiding material selection and designing anti-reflective coating to reduce reflection losses and enhance light harvesting. As the spectrum transitions into the IR region beyond 700 nm, a steady decrease in absorption is observed up to 2500 nm.[46]

In Fig. 1(b), the arc length represents the entire thickness of the PSC, while the electron–hole (e–h) generation rate quantifies the number of charge carriers produced by incident light, directly influencing the photocurrent and PCE. At an arc length near 1 nm, the e–h generation rate reaches its peak ($\sim$7.5 × 10^{21} cm^{-3} s^{-1}), mainly because the light is absorbed near the front interface where photon flux is maximum. As the arc length increases, the generation rate gradually decreases because the intensity of light attenuates with depth. In the deeper regions of the absorber layer, fewer photons remain available for absorption, resulting in a lower generation rate. At the maximum arc length, the generation rate approaches zero since most of the incident light has already been absorbed in the upper layer. Excessive thickness may also introduce additional series resistance and optical losses, negatively impacting overall device performance. Therefore, optimizing the arc length is essential to ensure efficient light absorption and carrier generation, ultimately enhancing solar cell output.[47]

Fig. 1(c) illustrates the correlation between SRH recombination (cm^{-3} s^{-1}) and arc length (nm), elucidating the impact of

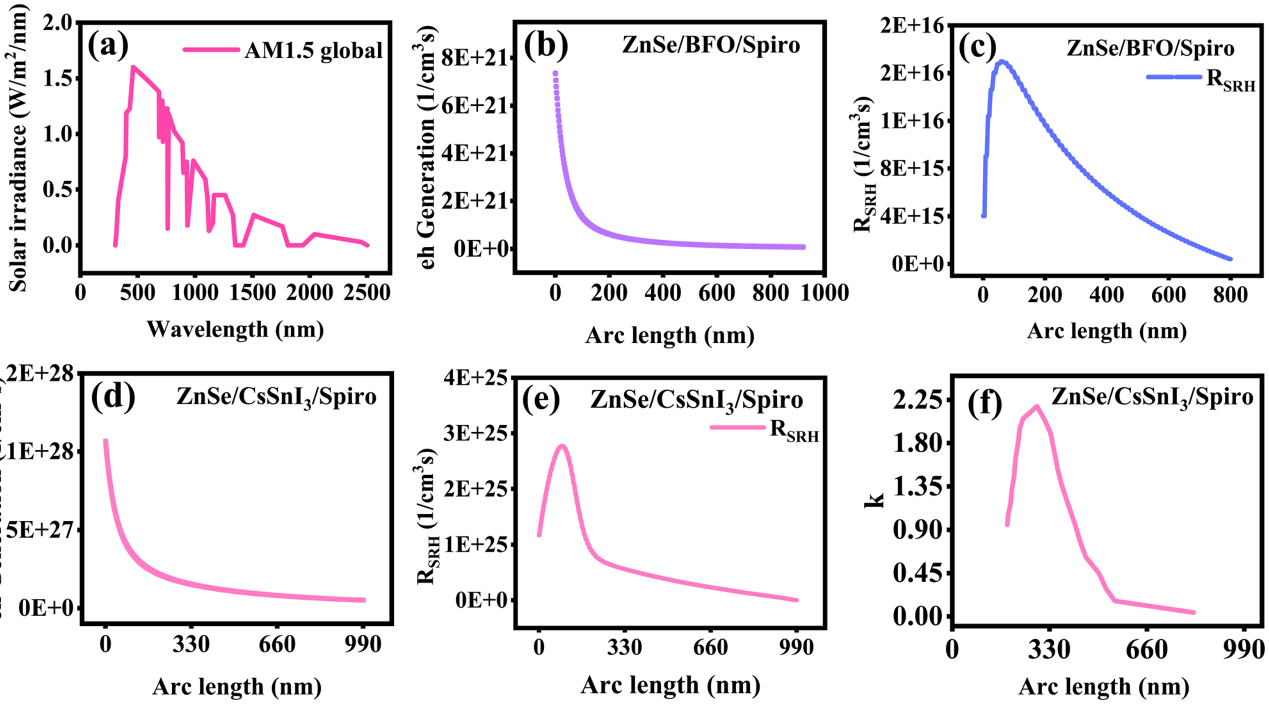

Fig. 1 (a) Distribution of solar irradiance in terms of wavelength describing the change in photon flux. (b) Dependence of electron–hole generation on BFO-based arc length. (c) Impacts of BFO-based arc length on the Shockley–Read–Hall recombination (R_{SRH}), optical and electrical profile across the ZnSe/CsSnI$_3$/spiro-OMeTAD structure, showing the (d) electron–hole generation rate, (e) Shockley–Read–Hall recombination (R_{SRH}) rate, and (f) extinction coefficient (k) as a function of CsSnI$_3$-based arc length.

recombination on solar cell performance. At minimum arc length, recombination remains relatively low ($\sim 4 \times 10^{15}$ cm^{-3} s^{-1}) due to the minimal carrier transport distance in thin absorber layers. At approximately 50 nm, recombination reaches a peak value of ($\sim 1.7 \times 10^{19}$ cm^{-3} s^{-1}), as carrier generation is maximized, and the reduced transport path within the thinner layer exacerbates the recombination rate. Furthermore, at lower thicknesses, a greater fraction of incident light reaches the absorber layer, thereby enhancing carrier generation. However, beyond this critical point, recombination gradually diminishes as arc length increases, attributed to the decline in carrier generation within the solar cell. At the maximum arc length, carrier generation becomes negligible as the incident light is unable to penetrate the absorber layer beyond a certain thickness, effectively reducing recombination to an insignificant level; in the absence of charge carriers, recombination ceases entirely.[48]

Fig. 1(d) shows the electron–hole generation rate as a function of arc length in a ZnSe/CsSnI$_3$/spiro layered solar cell structure. A sharp decline in generation rate with increasing arc length indicates that most photon absorption and carrier generation occur near the front surface, where light enters the device. This behavior aligns with the Beer–Lambert law, where light intensity decreases exponentially with depth due to strong absorption in the CsSnI$_3$ perovskite layer. It confirms that the device is optically optimized for front-side absorption and efficient charge generation. Fig. 1(e) shows the R_{SRH} along the arc length in the ZnSe/CsSnI$_3$/spiro solar cell structure. The peak near the front interface suggests a high density of trap-assisted recombination, likely due to defects at or near the ZnSe/CsSnI$_3$ interface. As the arc length increases, R_{SRH} gradually decreases, indicating fewer mid-gap trap states deeper within the absorber. This spatial distribution reflects the need for interface passivation to reduce recombination losses and improve overall device efficiency. Fig. 1(f) shows the variation of the extinction coefficient (k) with arc length in the CsSnI$_3$-based structure. The peak near 330 nm suggests strong optical absorption in the CsSnI$_3$ layer, which is due to the active absorber. After this point, k decreases steadily, indicating that light absorption weakens deeper into the device. This trend confirms that most light is absorbed in the central absorber region, enhancing photo-carrier generation.

3.2 Electronic energy band structure of the device

Fig. 2(a) illustrates the schematic architecture of the ZnSe/BFO/spiro-OMeTAD solar cell, where a multilayer configuration is strategically designed to optimize optical absorption and charge transport. The device is illuminated from the top through the transparent front contact, where light enters and is absorbed predominantly in the BFO layer, leading to the generation of e–h pairs. The electrons in the BFO layer are excited to the conduction band and move toward the ETL, while holes migrate toward the HTL. The movement pathways emphasize the role of each layer in selective charge extraction and recombination suppression. The thicknesses of each layer are optimized

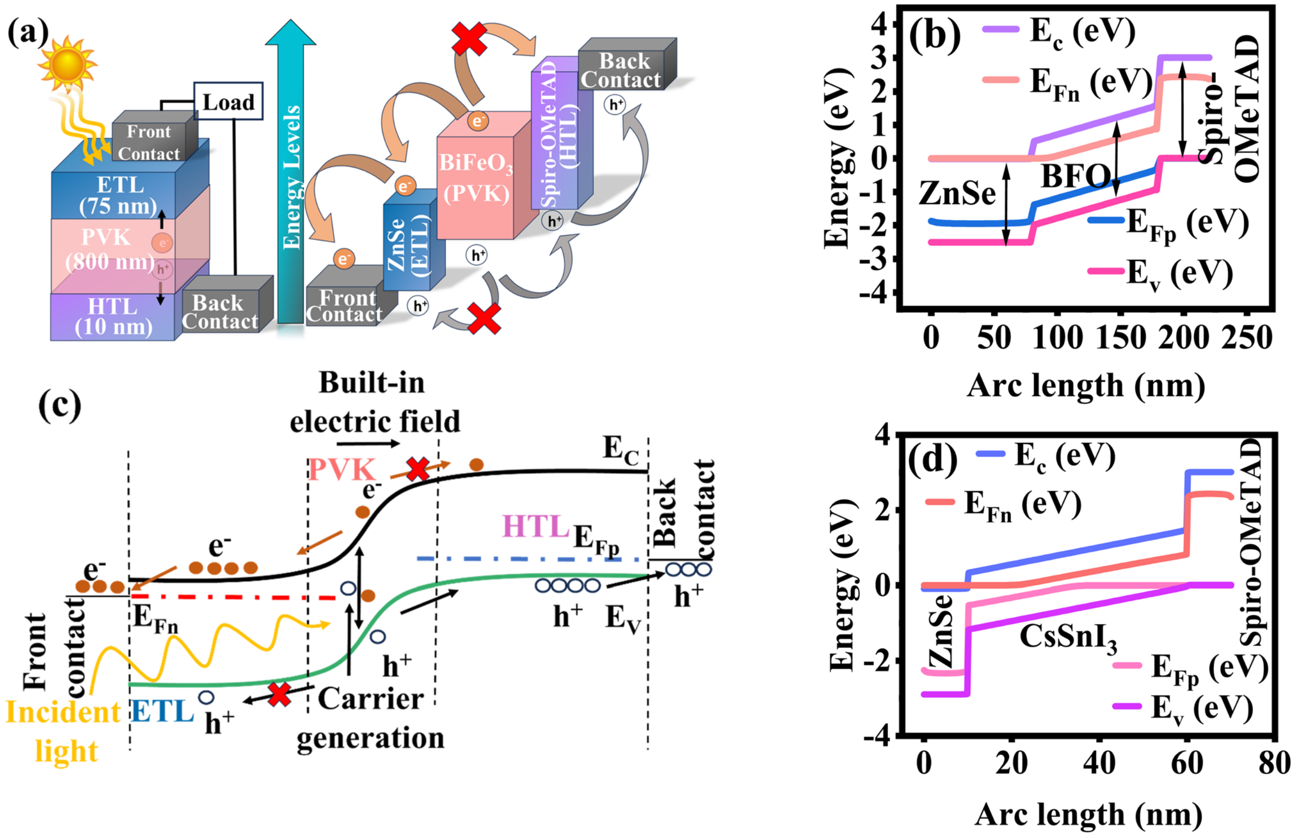

Fig. 2 (a) Structural layout of the proposed solar cell (ZnSe/BiFeO$_3$/spiro-OMeTAD). (b) The energy band diagram of the ZnSe/BFO/spiro-OMeTAD structure, showing alignment across each layer. (c) Visualization of the charge carrier flow and separation within the device. (d) The energy band diagram of the ZnSe/CsSnI$_3$/spiro structure, illustrating the band alignment and carrier transport pathways.

(75 nm for ETL, 800 nm for PVK layer, and 10 nm for HTL) to ensure maximum photon harvesting and efficient charge transport. The relative alignment of the conduction band (CB), valence band (VB), and Fermi energy levels of these materials with specifying their respective bandgap value, is illustrated in Fig. 2(b). The CB offset between BFO and spiro-OMeTAD enables hole transport. The careful engineering of band positions ensures minimal energy loss, efficient charge separation, and reduced carrier recombination, which are essential for achieving high PV performance. The energy band diagram under illumination, including the bending of energy bands due to built-in electric fields across interfaces, is shown in Fig. 2(c). This band bending promotes directional flow of e–h toward their respective contacts, enhancing charge collection. The incident light generates carriers within the absorber layer, and the electric field further assists in their rapid separation and transport, ultimately contributing to the overall efficiency of the solar cell. Fig. 2(d) shows the energy band alignment between the ETL (ZnSe), the absorber (CsSnI$_3$), and the HTL (spiro-OMeTAD), indicating the relative positions of their CB and VB. The CB of ZnSe is higher than that of CsSnI$_3$, allowing efficient electron transfer from the absorber to the ETL, while the VB of spiro-OMeTAD is above that of CsSnI$_3$, enabling smooth hole transport to the HTL. This favourable CB and VB alignment promotes directional charge flow, minimizes interfacial recombination, and improves overall device efficiency. The band diagram also reflects the integrated roles of each layer, whose distinct properties and bandgap are summarized in Table 1.[49]

4. Results and discussion

4.1 The effect of BFO's thickness variation in the ZnSe/BFO/spiro-OMeTAD solar cell

Fig. 3(a) schematically compares the impact of the BFO absorber's thickness on photogeneration dynamics within the solar cell. When the BFO layer is relatively thin, light absorption is incomplete, limiting the generation of e–h pairs and reducing photocurrent. Conversely, a thicker BFO layer enhances optical path length and photon absorption, thereby increasing the density of photo-generated carriers. However, excessively thick layers may introduce recombination losses and hinder charge extraction. This schematic underscores the importance of optimizing absorber thickness to balance efficient photogeneration with effective carrier transport. Fig. 3(b) presents the current density–voltage (J–V) curves for varying BFO thicknesses, revealing that as the absorber layer becomes thicker, the short-circuit current density (J_{sc}) increases due to improved light absorption and carrier generation. J_{sc} actually represents the current density flowing through the device when the

Table 1 Essential physical and electronic properties of the materials used in simulated BFO and $CsSnI_3$-based solar cell structures

Parameters	ZnSe (ETL)[16]	$BiFeO_3$ (absorber layer)[24]	$CsSnI_3$ (absorber layer)[65]	Spiro-OMeTAD (HTL)[24,36]
Thickness (nm)	75	800	990	10
Band gap (eV)	2.81	2.5	1.5	3
Electron affinity (eV)	4.09	3.3	3.5	1.9
Relative permittivity	8.60	6	9	3
Effective density of states at CB (cm^{-3})	2.2×10^{18}	5×10^{19}	1.8×10^{19}	1×10^{20}
Effective density of states at VB (cm^{-3})	1.9×10^{19}	5×10^{19}	2.2×10^{18}	1×10^{20}
Electron mobility ($cm^2\ V^{-1}\ s^{-1}$)	400	10	974	2
Hole mobility ($cm^2\ V^{-1}\ s^{-1}$)	110	25	213	1.0×10^{-2}
Electron lifetime (ns)	1	1000	1	5
Hole lifetime (ns)	1	1000	1	5

external voltage is zero, and it is directly linked to the number of photogenerated charge carriers collected at the electrodes. However, the onset of the current drop shifting with thickness occurs at 2.1 V for thinner films and around 1.9 V for thicker ones. This shift reflects changes in the internal electric field and increased recombination at larger thicknesses, influencing the charge extraction and overall device performance. Fig. 3(c) illustrates the power–voltage (P–V) characteristics for different BFO thicknesses. As the absorber thickness increases, maximum output power (P_{max}) also increases, while the peak power voltage drops from ~2.1 V for thinner layers to ~1.9 V for thicker ones. This decline is attributed to increased series resistance and recombination losses at higher thicknesses, which hinder efficient charge transport and slightly reduce the operating voltage.[50,51]

Fig. 3(d) further illustrates that J_{sc} increases from 4.44 to 7.63 mA cm^{-2} with thickness owing to improved photon absorption, whereas open-circuit voltage (V_{oc}) decreases from 2.14 to 1.93 V due to the concomitant rise in charge carrier recombination, defect density, and trap states. V_{oc} is the maximum voltage a solar cell can provide under open-circuit conditions, which reflects the difference between the quasi-Fermi levels of electrons and holes and is strongly dependent on the absorber bandgap and recombination losses. Similarly, P_{max} initially increases as a result of enhanced absorption and reduced recombination losses but subsequently declines beyond the optimal thickness (~800 nm) due to the prevalence of excessive trap states and heightened recombination rates. Fig. 3(e) depicts the dependence of PCE and FF on BFO thickness, where FF decreases from 73.33% to 63.6% with increasing thickness, primarily due to elongation of the carrier transport path, which induces higher resistive losses and exacerbates recombination. The PCE exhibits an initial enhancement with increasing thickness, reaching its peak at 800 nm, from 7.03% to 9.43% where optimal photon absorption, minimized recombination losses, and favourable carrier transport pathway collectively

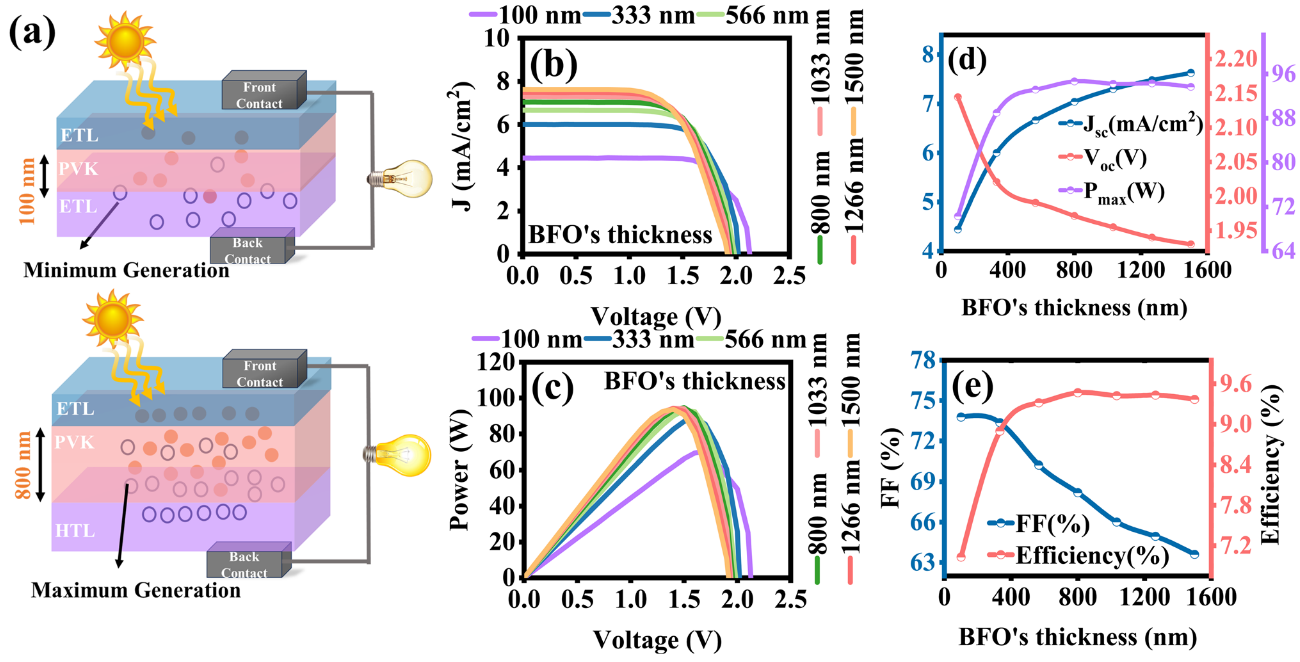

Fig. 3 (a) Schematic showing the comparison between two different thicknesses of the BFO layer in the ZnSe/$BiFeO_3$/spiro-OMeTAD solar cell. (b and c) J–V & P–V characteristics, and (d and e) the impact of BFO thickness variation on PV parameters such as J_{sc}, V_{oc}, P_{max}, FF, and efficiency.

Table 2 Influence of the absorber layer's thickness on the photovoltaic performance of the ZnSe/BiFeO$_3$/spiro-OMeTAD device

BFO's thickness (nm)	J_{sc} (mA cm^{-2})	V_{oc} (V)	P_{max} (W)	FF%	Efficiency%
100	4.44	2.14	70.30	73.77	7.03
333	6.00	2.02	88.97	73.36	8.89
566	6.66	1.99	93.17	70.22	9.31
800	7.04	1.97	94.66	68.18	9.46
1033	7.30	1.95	94.22	66.00	9.42
1266	7.48	1.93	94.30	64.93	9.43
1500	7.63	1.93	93.67	63.60	9.36

contribute to performance maximization. However, beyond this optimal thickness, PCE declines due to the extension of the carrier transport path, which fosters recombination and resistive dissipation.[52] The variation in BFO thickness results in a complex interplay among photovoltaic parameters, validating the implication of thickness-induced perturbation in charge carrier transport dynamics, as summarized in Table 2.

4.2 The effect of ETL thickness variation in the ZnSe/BFO/spiro-OMeTAD solar cell

In Fig. 4(a), the variation in ETL thickness markedly influences electron extraction. A thinner ETL provides a shorter transport path and lower bulk resistance, which accelerates electron drift-diffusion toward the electrode and improves charge collection efficiency. The reduced thickness also enhances the interfacial electric field, suppressing recombination at the ETL/absorber interface. In contrast, an excessively thick ETL introduces higher series resistance and elongated carrier pathways, which not only slow down electron mobility but also increase the probability of trap-assisted recombination. Furthermore, thicker ETLs can misalign the energy band bending at the interface, thereby weakening charge selectivity and deteriorating the V_{oc} and FF. As a result, optimizing ETL thickness is crucial to balance optical absorption, transport dynamics, and interfacial charge separation for achieving maximum device efficiency. In Fig. 4(b), the *J*–*V* characteristics reveal that the built-in electric field remains nearly constant across all ETL thicknesses, indicating stable internal electric field conditions. However, with increasing ETL thickness, a noticeable shift occurs in the voltage at which the *J* begins to drop sharply. Specifically, the drop is observed at 2 V for 100 nm and shifts to 2.2 V for 125 nm, suggesting increased resistive losses or delayed carrier extraction in thicker ETLs, which negatively affects the charge transport dynamics under forward bias.[53] A similar trend is evident in the *P*–*V* curves presented in Fig. 2(c), where increasing ETL thickness leads to a rightward shift in the peak power voltage, reflecting delayed carrier collection and increased resistive losses.[54]

In Fig. 4(d), J_{sc} increases from 0.82 to 0.83 mA cm^{-2} until 100 nm, then decreases to 0.82 mA cm^{-2} due to the carrier path length at higher ETL thickness (125 nm), whereas V_{oc} increases from 1.96 V to 2.20 V owing to improved band alignment, enhanced electron extraction, and better hole-blocking efficiency. The highest P_{max} of 102.32 W is achieved at an optimal thickness of 75 nm, where efficient charge transport minimizes recombination losses; however, beyond this point, P_{max} decreases as excessive ETL thickness prolongs the electron path, intensifying recombination losses.[42] Fig. 4(e) illustrates that both FF (∼61.91%) and PCE (∼10.72%) improve as the ETL thickness increases up to the optimal value, primarily due to enhanced photocurrent generation. The improvement results from increased light absorption in the absorber layer, efficient electron extraction, reduced non-radiative recombination

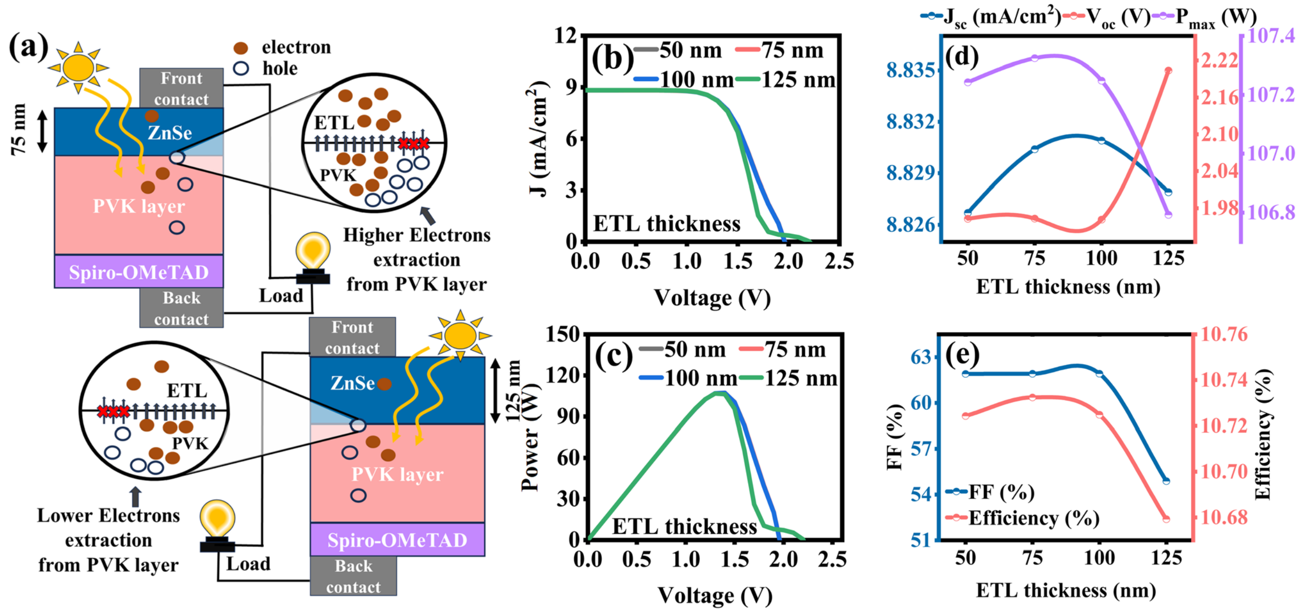

Fig. 4 (a) Schematic visualization of the ZnSe/BiFeO$_3$/spiro-OMeTAD solar cell with varied ETL thicknesses. (b and c) *J*–*V* & *P*–*V* characteristics, and (d and e) the effect of the ETL thickness variation on PV parameters such as J_{sc}, V_{oc}, P_{max}, FF, and efficiency.

Table 3 Influence of the ETL thickness variation on the photovoltaic output of the ZnSe/BiFeO$_3$/spiro-OMeTAD solar cell

ETL thickness (nm)	J_{sc} (mA cm^{-2})	V_{oc} (V)	P_{max} (W)	FF%	Efficiency%
50	8.82	1.96	107.24	61.90	10.72
75	8.83	1.96	107.32	61.91	10.73
100	8.83	1.96	107.24	61.91	10.72
125	8.82	2.20	106.79	54.88	10.67

losses, high transparency, and minimized series resistance (R_s). However, beyond the optimal thickness, resistive losses escalate due to poor band alignment, extended electron pathways, increased recombination, and hindrance to photon penetration in the absorber layer.[20,55] Table 3 evaluates the impact of ETL thickness variation (~50 nm to ~125 nm) on solar cell performance, emphasizing the dependence of PV parameters on the material's thickness.

4.3 The effect of HTL thickness variation in the ZnSe/BFO/spiro-OMeTAD solar cell

In Fig. 5(a), the influence of HTL thickness on device performance is evident. A thinner HTL promotes efficient hole extraction by minimizing transport resistance, shortening carrier pathways, and enhancing the interfacial electric field, thereby reducing recombination probability. However, as the HTL thickness increases, the longer transport distance and higher bulk resistance hinder hole mobility, weaken the interfacial driving force, and promote charge accumulation, which collectively degrade the extraction efficiency and overall photovoltaic performance. As shown in Fig. 5(b), increasing HTL thickness results in a noticeable decrease in J_{sc}, and the voltage at which J drops shifts from 2.0 V (lower thickness) to 1.9 V (higher thickness), indicating degraded carrier extraction and increased resistive effects.[56] A similar trend appears in the P–V curves as shown in Fig. 5(c), where the peak power voltage shifts toward lower values with thicker HTLs, confirming reduced charge collection efficiency and overall performance deterioration.[57]

Fig. 5(d) demonstrates that with an HTL thickness of 10 nm, the maximum values of J_{sc} (~8.82 mA cm^{-2}), V_{oc} (~1.96 V), and P_{max} (~107.24 W) are achieved due to enhanced hole extraction, minimized recombination losses, and reduced resistive losses enabled by smooth band alignment. However, beyond 10 nm, three parameters (J_{sc}, V_{oc}, and P_{max}) degrade as holes encounter challenges in reaching the back electrode, resulting in increased interfacial recombination, poor band alignment with the absorber layer, and elevated resistive losses.[58,59] Fig. 5(e) investigates the impact of HTL thickness on FF and PCE, revealing that FF increases with thickness, attaining a peak value of ~65.04% at 150 nm due to enhanced band alignment, reduced resistive losses, lower recombination, efficient hole extraction, and higher shunt resistance (R_{sh}). Conversely, PCE reaches its maximum value of ~10.72% at a lower HTL thickness of ~10 nm, attributed to reduced resistance and minimal charge carrier recombination. Beyond this thickness, PCE diminishes due to an extended hole transport pathway, intensified carrier recombination, reduced charge carrier generation, inefficient charge collection at the electrode, and increased R_s, leading to power losses.[37,60] Increasing the HTL thickness causes a complex response in PV parameters, highlighting the wide implications of thickness perturbation in charge carrier transport dynamics, as summarized in Table 4.

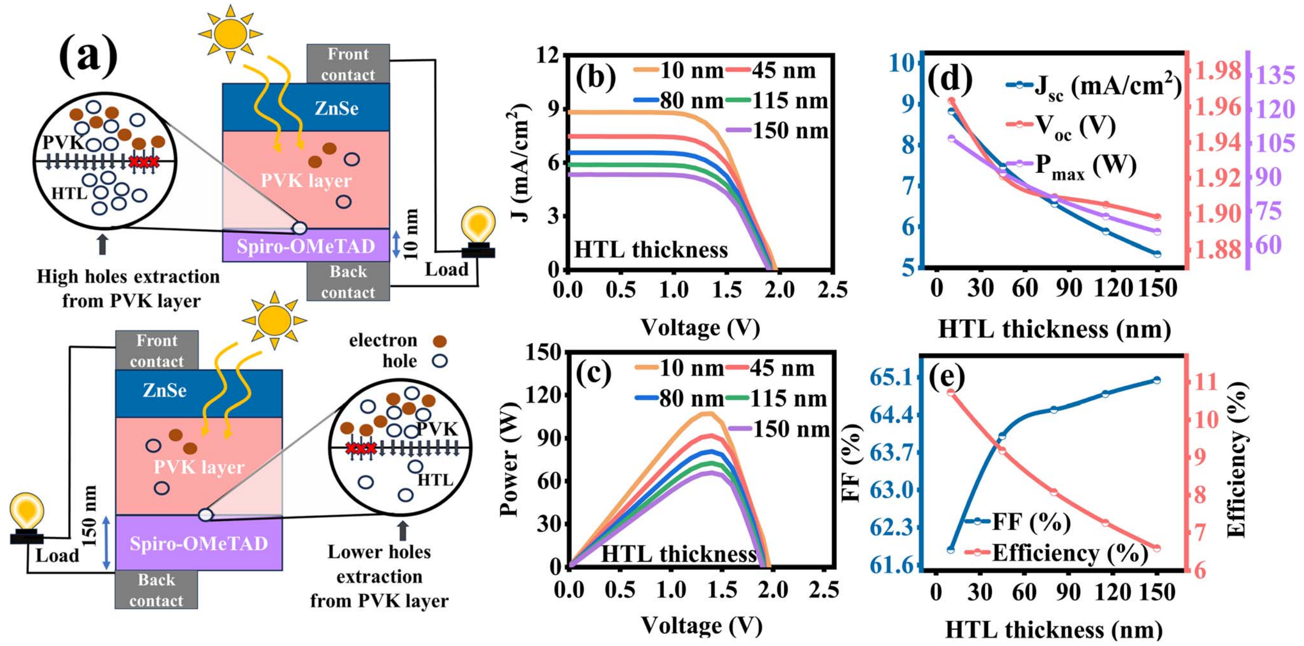

Fig. 5 (a) Schematic of the solar cell with different absorbing layer thicknesses. (b and c) J–V & P–V characteristics, and (d and e) the influence of HTL thickness variation on PV parameters such as J_{sc}, V_{oc}, P_{max}, FF, and efficiency.

Table 4 Variation in device performance with changing HTL thickness in the ZnSe/BiFeO_3/spiro-OMeTAD solar cell

HTL thickness (nm)	J_{sc} (mA cm^{-2})	V_{oc} (V)	P_{max} (W)	FF%	Efficiency%
10	8.82	1.96	107.24	61.88	10.72
45	7.47	1.92	91.85	64.00	9.18
80	6.55	1.90	80.76	64.49	8.07
115	5.88	1.90	72.61	64.78	7.26
150	5.33	1.89	65.84	65.04	6.58

4.4 The effect of acceptor/donor density gradients in ZnSe/BFO/spiro-OMeTAD solar cell

Fig. 6(a) represents the schematic structure of the perovskite solar cell, highlighting the donor density (N_D) in the ETL and the acceptor density (N_A) in the HTL. Upon illumination, the PVK absorber generates charge carriers, where electrons are driven toward the ETL and holes toward the HTL. The respective donor and acceptor densities control the charge transport, extraction efficiency, and overall device performance. In Fig. 6(b), the minimum J_{sc} of 7.04 mA cm^{-2} is observed when the N_A exceeds 1×10^{17} cm^{-3}, indicating reduced charge extraction due to enhanced recombination. Conversely, J_{sc} increases with increasing N_D. The minimum J_{sc} of 7.54 mA cm^{-2} occurs when the N_A lies between 1×10^{14} and 1×10^{16} cm^{-3}, and the N_D is in the range of 1×10^{18} and 1×10^{20} cm^{-3}, reflecting optimal carrier balance and efficient transport. Fig. 6(c) illustrates that the V_{oc} remains below 1.88 V for doping concentrations below 1×10^{19} cm^{-3}, primarily due to low built-in potential and substantial recombination losses. With increasing doping density, V_{oc} exhibits a modest enhancement, reaching a peak of 1.97 V at 1×10^{20} cm^{-3}, attributed to improved band bending and suppressed recombination. However, increasing doping levels enhances recombination, a non-radiative process that ultimately imposes a strict upper limit on V_{oc}. Fig. 6(d) demonstrates that the P_{max} is initially at a minimum of approximately 65 W under low doping conditions due to pronounced recombination effects. As the N_A exceeds 1×10^{18} cm^{-3}, P_{max} exhibits a marginal increase to 87.18 W, followed by a decline attributed to recombination. Excessive doping beyond this point results in diminished P_{max} due to elevated recombination, where phonons are emitted instead of light. At an optimal doping level of 1×10^{20} cm^{-3} for N_A & N_D, the P_{max} reaches a peak value of 94.7 W, attributed to an optimal doping concentration that enhances bend bending while mitigating recombination and R_S.[61]

In Fig. 6(e), the FF is lowest (~47.30%) when the N_A is below 1×10^{17} cm^{-3}, indicating poor charge collection and imbalance. As the N_A increases beyond 1×10^{17} cm^{-3}, FF steadily improves. The highest FF (~68.30%) is achieved when N_A/N_D lies between 1×10^{19} and 1×10^{20} cm^{-3}, reflecting optimal charge transport and reduced recombination within the PSC. Fig. 6(f) reveals that the PCE is at its lowest under doping conditions, primarily due to the constrained built-in potential and elevated recombination rate. As the N_A surpasses 1×10^{18} cm^{-3}, PCE increases to 8.71%, driven by enhanced carrier mobility, improved built-in potential, and reduced recombination.[37,57] The PCE reaches its peak value of 9.47% at a doping concentration of 1×10^{20} cm^{-3} due to optimized doping that enhances carrier collection, but further doping increases carrier scattering and recombination, leading to PCE degradation. These findings highlight the implication of N_D & N_A gradients in charge carrier transport dynamics to improve the efficiency of the device.

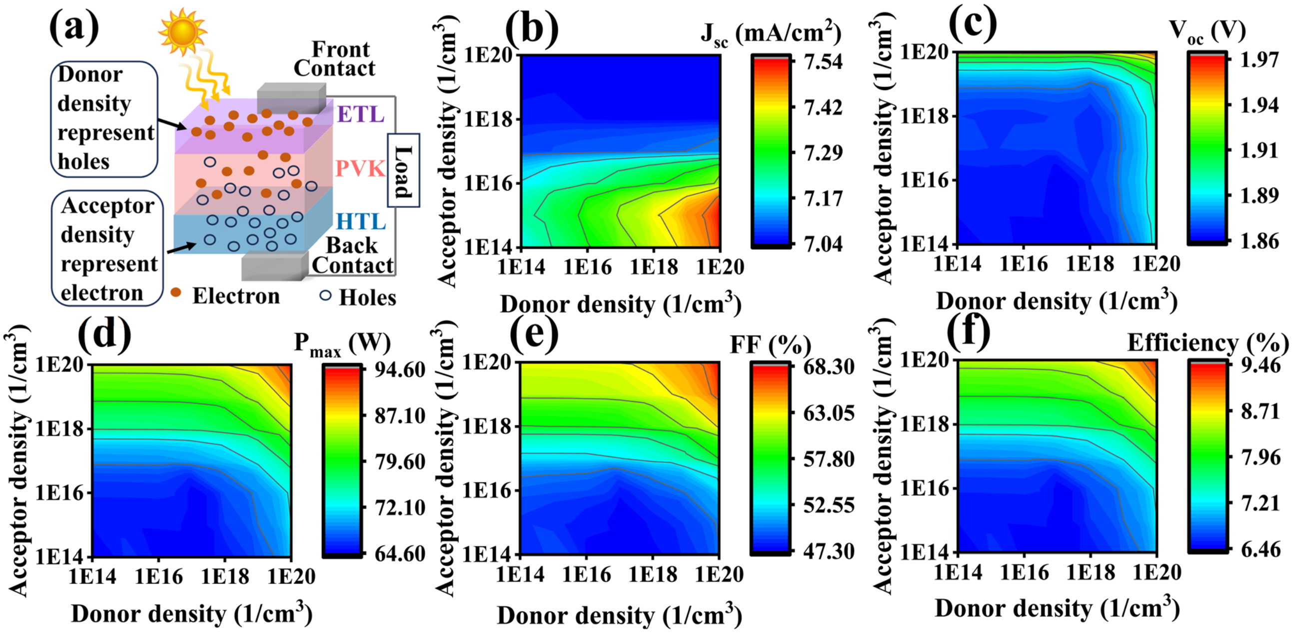

Fig. 6 (a) Schematic depiction of donor and acceptor concentrations, highlighting their role in performance; (b–f) corresponding trends in PV performance metrics with varying carrier densities, such as J_{sc}, V_{oc}, P_{max}, FF, and efficiency, respectively.

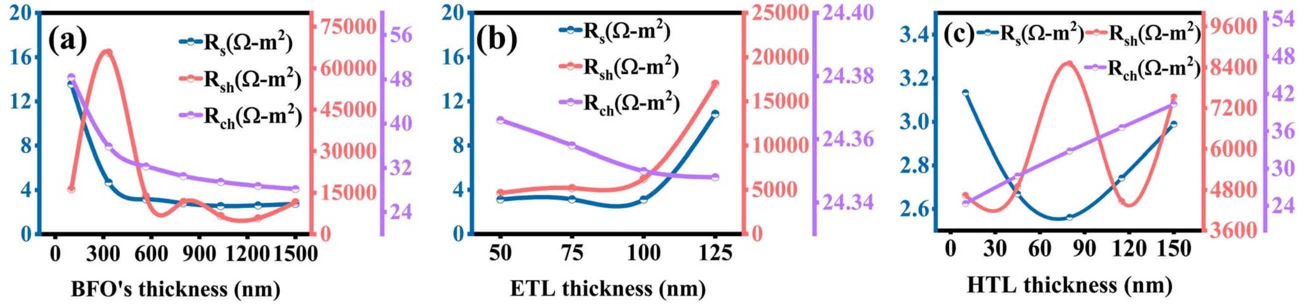

Fig. 7 Variation in series resistance (R_s), shunt resistance (R_{sh}), and characteristic resistance (R_{ch}) with respect to the (a) absorbing layer (BFO) thickness, (b) ETL thickness, and (c) HTL thickness.

4.5 The impact of layer thickness variation on the resistance in the ZnSe/BFO/spiro-OMeTAD solar cell

Fig. 7(a) elucidates the correlation between these resistances, *i.e.*, R_s, R_{sh}, and the characteristic resistance (R_{ch}), and the variation in the BFO thickness of 100 nm. R_s exhibits a significantly high value (~14 Ω m^2) due to the presence of interfacial defects, the intrinsic resistivity of the BFO layer, and increased charge carrier recombination. However, with a progressive increase in thickness, R_s significantly declines (~3 Ω m^2) as defect density is mitigated by the optimal selection of solvents. A higher R_{sh} (~65 625 Ω m^2) is preferred for superior PSC performance, and its values remain favourable across different BFO thicknesses, peaking at ~333 nm, which ensures optimal efficiency.[62] R_{ch}, a critical parameter indicating overall PSC efficiency and device quality, reaches a peak value of ~48.39 Ω m^2 at a minimum thickness of ~100 nm.

Fig. 7(b) presents the variation of R_s, R_{sh}, and R_{ch} with ETL thickness, where a minimal R_s is essential for efficient PSC performance, attaining its lowest value (~3.11 Ω m^2) at 100 nm thickness, attributed to reduced interfacial defect density. At 125 nm thickness, R_s increases (~10.85 Ω m^2), resulting in performance deterioration due to intensified charge carrier recombination. The maximum R_{sh} (~16 988 Ω m^2) occurs at 125 nm thickness; however, at 75 nm, R_{sh} remains sufficiently high due to enhanced current transport and reduced recombination, facilitated by the minimized R_s at this thickness.[62] The highest R_{ch} (~24.36 Ω m^2) is recorded at 50 nm ETL thickness, beyond which subsequent variations exert minimal influence, inducing a slight decline in performance, while PSC efficiency reaches its optimum at an ETL thickness of approximately 125 nm.

Fig. 7(c) illustrates the dependence of R_s, R_{sh}, and R_{ch} on the variation in HTL thickness, highlighting the relationship between electrical resistance and material properties. The minimum R_s (~2.5 Ω m^2) at 80 nm HTL thickness is attributed to crystal defects and reduced grain size, which coincides with optimal R_{sh} (~8505 Ω m^2) at the same thickness, thereby enhancing both J_{sc} and V_{oc}.[63] For HTL thicknesses exceeding 80 nm, R_{sh} progressively increases as the internal and fabrication-related defects diminish, although peak efficiency is attained precisely at 80 nm thickness.[62] R_{ch} exhibits a linear increase with HTL thickness; however, its effect on overall PSC performance remains negligible, as the highest PCE is achieved at 10 nm thickness. The extracted resistance values, derived through Python-based simulation, lie within the optimized operational range, ensuring reliable and efficient PSC performance.

In our simulations, the increase in FF with optimized HTL thickness is not a simple geometrical effect, but arises from the interplay between recombination dynamics and band alignment at the absorber/HTL interface. A very thin HTL leads to incomplete coverage and poor hole extraction, which enhances interfacial recombination and increases series resistance, both of which reduce FF. On the other hand, when the HTL thickness is gradually increased to the optimum range, it provides smoother band alignment and more efficient separation of carriers. This reduces interfacial recombination and improves charge collection, thereby increasing the FF.

However, beyond the optimum thickness, the FF begins to saturate or even decrease slightly because excessive HTL thickness contributes to increased series resistance, which counteracts the benefits of improved carrier extraction. Thus, the observed "direct relation" between FF and HTL thickness should be understood as a balance: FF improves with HTL thickness up to an optimum level because of reduced recombination and enhanced band alignment, but excessive thickness may introduce resistive losses.

4.6 The impact of layer thicknesses on the ZnSe/CsSnI$_3$/spiro-OMeTAD solar cell

In Fig. 8(a), the *J*–*V* curves demonstrate that increasing the CsSnI$_3$ absorber thickness results in a pronounced rise in J_{sc}, with thinner layers showing a current density drop near 1.0 V, whereas thicker layers exhibit this drop around 0.7 V. This shift, coupled with the overall enhancement in photocurrent, reflects the improved light absorption capacity of thicker CsSnI$_3$ films, enabling more efficient photocarrier generation. In Fig. 8(b), the *P*–*V* characteristics indicate that increasing the CsSnI$_3$ thickness significantly enhances P_{max}, with thinner layers showing a pronounced power drop near 1.0 V, while thicker layers exhibit this drop shifted toward approximately 0.7 V. The sustained high-power output at lower voltages for thicker absorbers can be attributed to improved photon absorption and carrier collection, which outweigh the slight V_{oc} reduction

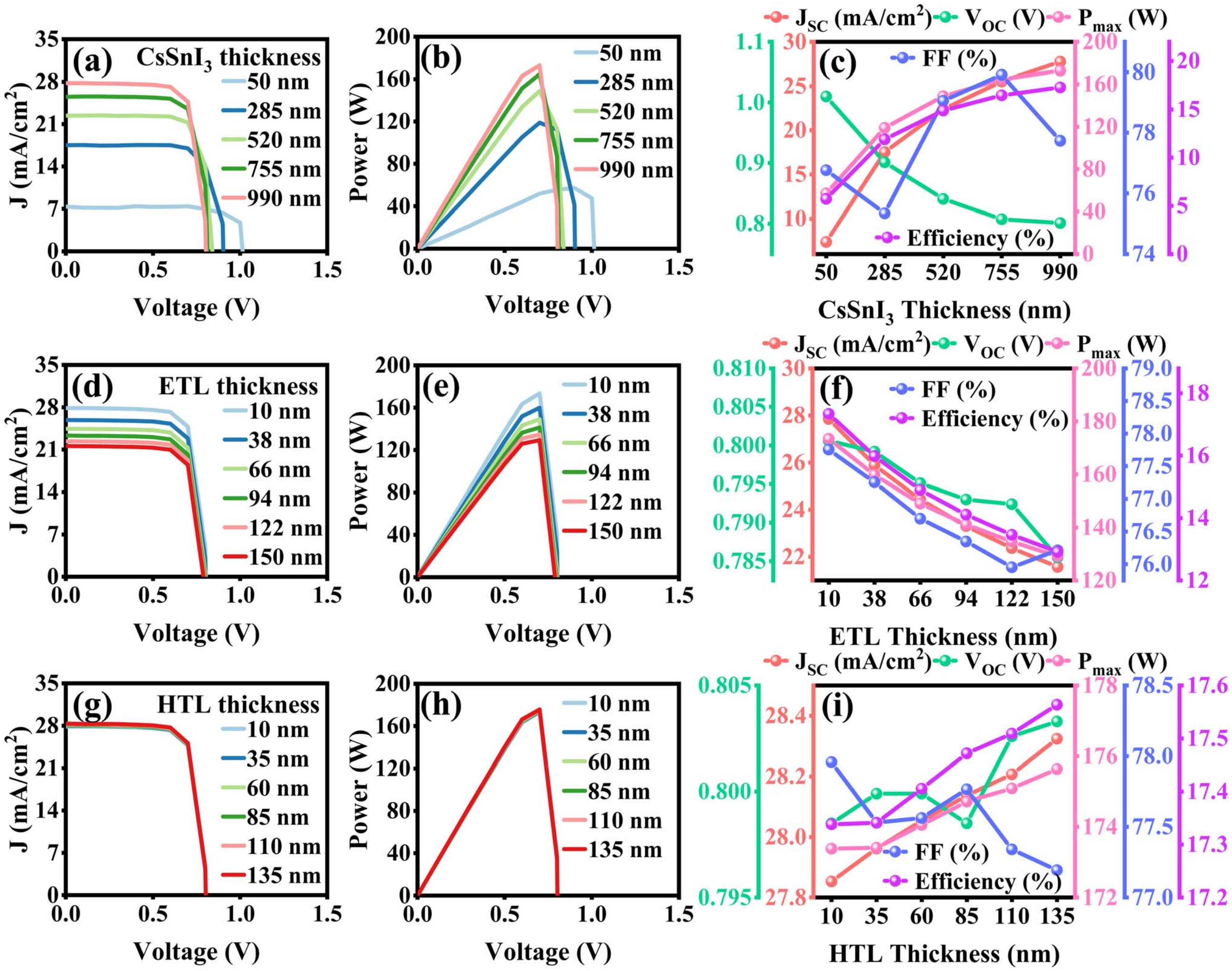

Fig. 8 (a–c) Effect of absorber layer ($CsSnI_3$) thickness variation on *J–V* characteristics, *P–V* characteristics, and trends in J_{sc}, V_{oc}, P_{max}, FF, and efficiency. (d–f) The influence of ETL thickness on *J–V* characteristics, *P–V* characteristics, and trend in J_{sc}, V_{oc}, P_{max}, FF, and efficiency. (g–i) The impact of HTL thickness variation on *J–V* characteristics, *P–V* characteristics, and trends in J_{sc}, V_{oc}, P_{max}, FF, and efficiency.

caused by increased recombination pathways. In Fig. 8(c), J_{sc} increases from 7.36 mA cm^{-2} at 50 nm to 27.75 mA cm^{-2} at 990 nm, primarily due to enhanced optical path length in thicker $CsSnI_3$ layers, which improves photon absorption and generates more e–h pairs.[50,51] V_{oc} decreases from 1.01 to 0.80 V with increasing thickness, as longer carrier transport distances and increased defect density promote bulk and interfacial recombination, reducing the quasi-Fermi level splitting. P_{max} rises from 57.12 to 172.88 W, and FF remains relatively stable between 75.34 and 79.91%, indicating that series resistance and charge extraction remain efficient despite thickness variation. The overall efficiency improves from 5.71 to 17.28% because the gain in J_{sc} and P_{max} outweighs the V_{oc} drop (see Table 1S in the SI), highlighting that thicker absorbers effectively balance absorption enhancement with manageable recombination losses.

The *J–V* curves in Fig. 8(d) indicate that increasing ETL thickness leads to a gradual decrease in J_{sc}, as thicker layers introduce longer transport paths and higher series resistance, reducing carrier extraction efficiency. For all thicknesses, the current density drop occurs consistently at ~0.8 V, reflecting a nearly unchanged V_{oc}. The *P–V* curves in Fig. 8(e) display a steady reduction in P_{max} with greater ETL thickness, while the voltage point at which the power drop occurs remains fixed at ~0.8 V. This behavior suggests that the decline in power output is mainly governed by the reduced photocurrent rather than significant voltage loss.[52,53] In Fig. 8(f), J_{sc} decreases from 27.85 mA cm^{-2} at 10 nm to 21.57 mA cm^{-2} at 150 nm, mainly due to increased optical losses, longer transport paths, and higher series resistance in thicker ETLs, which limit carrier extraction. V_{oc} shows only a slight reduction from 0.80 to 0.78 V, indicating minimal effect on energy band alignment. P_{max} declines from 173.38 to 129.16 W, and efficiency drops from 17.33 to 12.91%, with both trends following the reduction in J_{sc}. FF remains relatively stable between 75.95 and 77.75%, reflecting preserved diode quality despite the transport limitations imposed by thicker ETLs. This behaviour confirms that thinner ETLs provide superior performance by reducing resistive losses and enabling more efficient carrier collection (see Table 2S in the SI).

Table 5 Comparative analysis of BFO-based perovskite solar cells reported in various research studies for efficient solar cell design

Cell structure	J_{sc} (mA cm^{-2})	V_{oc} (V)	FF%	Efficiency%
FTO/TiO_2/BFO/spiro-OMeTAD[1]	10.87	0.91	55.55	5.60
FTO/ZnO/BFO[21]	15.27	1.03	75.59	11.92
ZnO/BFO/spiro-OMeTAD[24]	8.99	2.00	65.47	11.87
FTO/ZnO/BFO/spiro-OMeTAD/Au[27]	8.35	0.79	29.10	1.92
ZnSe/BFO/spiro-OMeTAD [this work]	8.83	1.96	61.91	10.73

The *J–V* curves in Fig. 8(g) show that increasing HTL thickness produces only a very minor rise in J_{sc}, indicating that hole transport is already efficient at lower thicknesses. For all thicknesses, the current density drop occurs consistently at ∼0.8 V, suggesting a negligible effect on V_{oc}. The *P–V* curves in Fig. 8(h) exhibit a slight increase in P_{max} with greater HTL thickness, while the voltage at which the power drop occurs remains fixed at ∼0.8 V. This trend implies that any performance gain is marginal and is mainly linked to the minor photocurrent enhancement. Fig. 8(i) displays that as HTL thickness increases from 10 to 135 nm, J_{sc} rises only slightly from 27.85 to 28.32 mA cm^{-2}, reflecting minimal improvement in light absorption or carrier extraction.[64] V_{oc} remains stable at 0.79 V for thinner layers and increases marginally to 0.80 V for thicker ones, indicating consistent band alignment. P_{max} grows from 173.38 to 175.63 W, and efficiency increases marginally from 17.33 to 17.56%, while FF stays between 77.19% and 77.95%, confirming that HTL thickness variation has little influence on diode quality or charge transport.[57] Overall (see Table 3S in the SI), performance changes are negligible, suggesting that the device operates near optimal HTL thickness, even at the lowest tested value.

A comparative analysis of BFO-based solar cells is clearly tabulated in Table 5, showing that device performance varies significantly with changes in ETLs and HTLs. The FTO/ZnO/BFO/spiro-OMeTAD/Au cell delivers very low PCE (1.92%) due to weak FF and limited V_{oc}, reflecting poor carrier extraction and higher recombination.[33] The TiO_2-based structure moderately improves PCE (5.60%), but still lacks high voltage output, indicating insufficient band alignment.[1] In ZnO/BFO/spiro-OMeTAD, the device without FTO showed improved V_{oc} (2.0 V) and FF, leading to an efficiency of 11.87%, suggesting reduced interface losses.[30] Interestingly, the FTO/ZnO/BFO structure without HTL showed the highest J_{sc} (15.27 mA cm^{-2}) and maximum PCE (11.92%), but the absence of HTL may affect long-term charge separation and stability.[27] In contrast, our work proposes a novel structure ZnSe/BFO/spiro-OMeTAD, which achieves a very high V_{oc} (2.20 V) and FF (73.77%), resulting in a stable efficiency of 10.73%. The use of ZnSe as an ETL is a key novelty, offering better energy level alignment and stronger electron mobility compared to traditional ZnO or TiO_2. This not only ensures effective electron extraction but also reduces recombination at the ETL/BFO interface. The non-toxic nature of ZnSe and BFO makes our configuration environmentally friendly, while the achieved performance parameters confirm the potential of this novel structure as a promising candidate for high-voltage, lead-free solar devices.

5. Conclusion

In this study, the operational power conversion efficiencies (PCE) of two lead (Pb)-free perovskite solar cells (PSCs) were simulated using the COMSOL Multiphysics software in a two-dimensional (2D) framework. The impact of the absorber layer, electron transport layer (ETL) (ZnSe), and hole transport layer (HTL) (spiro-OMeTAD) thickness variations, along with acceptor and donor density (N_A/N_D) gradient, on device performance with the ZnSe/$BiFeO_3$/spiro-OMeTAD architecture was analysed. By varying the absorber thickness from ∼100 nm to ∼1500 nm, optimum performance was achieved at 800 nm, where short-circuit current density (J_{sc}) reached 7.63 mA cm^{-2}, maximum output power (P_{max}) was 94.6 W, and PCE peaked at 9.46%. However, open-circuit voltage (V_{oc}) and fill factor (FF) declined from 2.14 V to 1.93 V and from 73% to 63%, respectively. When the ETL thickness was varied between 50 nm and 125 nm, V_{oc} improved significantly (1.96 V to 2.21 V) with a relatively stable J_{sc} ∼ 8.83 mA cm^{-2}. However, P_{max} and PCE showed minor reductions, with FF decreasing from 61.90% to 54.67%, and PCE dropping slightly from 10.72% to 10.69%. HTL thickness variation from 10 nm to 150 nm resulted in optimal photovoltaic performance at 10 nm, yielding J_{sc} ∼ 8.82 mA cm^{-2}, V_{oc} ∼ 1.96 V, P_{max} ∼ 107.2 W, and PCE ∼ 10.72%, while the maximum FF (∼53%) was achieved at 150 nm. For the ZnSe/$CsSnI_3$/spiro-OMeTAD cell, a maximum efficiency of 17.56% and J_{sc} of 28.32 mA cm^{-2} were obtained at 135 nm HTL thickness, FF of 79.91% at optimum $CsSnI_3$ thickness, and V_{oc} of 1.01 V at 10 nm $CsSnI_3$ thickness. Furthermore, by increasing N_A/N_D from 1×10^{14} to 1×10^{20} cm^{-3}, the PCE rose from 6.49% to 9.46%, FF increased from 48% to 68%, and V_{oc} went from 1.86 V to 1.97 V. Additionally, characteristic series and shunt resistances were investigated under varied layer thicknesses using Python simulations. The optimized resistance values support enhanced charge transport and reduced recombination losses, further validating the device design. This study highlights the linear relation between FF and HTL thickness, paving the pathway to selecting the best photovoltaic materials at optimized conditions for green energy solutions.

Conflicts of interest

There are no conflicts to declare.

Data availability

Data will be made available on request.

Supplementary information: A detailed investigation of the $CsSnI_3$-based solar cell, including performance parameters and simulation results. The study tables presented therein offer extended insights that complement the main text and enable an in-depth evaluation of the device behavior. See DOI: **https://doi.org/10.1039/d5ra06410d**.

Acknowledgements

The authors would like to acknowledge Ongoing Research Funding Program, (ORF-2025-1385), King Saud University, Riyadh, Saudi Arabia.

References

1 A. Raj, S. Sharma, D. V. Singh, A. Kumar, R. K. Chourasia, J. M. Siqueiros, O. R. Herrera, A. Anshul and M. Kumar, *Phys. B*, 2024, **673**, 415504.
2 J. L. Holechek, H. M. Geli, M. N. Sawalhah and R. Valdez, *Sustainability*, 2022, **14**, 4792.
3 M. Mobaseri, S. N. Mousavi and M. H. M. Haghighi, *Caspian J. Environ. Sci.*, 2021, **19**, 601–618.
4 M. Sajid, K. Ali, H. S. Shah, A. Shahid, S. A. Bakar, M. Yousaf and S. L. Lee, *J. Opt.*, 2024, 1–12.
5 J. A. Owolabi, M. Y. Onimisi, J. A. Ukwenya, A. B. Bature and U. R. Ushiekpan, *Am. J. Phys. Appl.*, 2020, **8**, 8–18.
6 A. Tolón-Becerra, X. Lastra-Bravo and F. Bienvenido-Bárcena, *Renewable Energy*, 2011, **36**, 2067–2077.
7 S. K. Pata and M. Balcilar, *Environ. Sci. Pollut. Res.*, 2024, **31**(21), 31304–31313.
8 K. G. Beepat, D. P. Sharma, D. Pathak and A. Mahajan, *Int. J. Mod. Phys. B*, 2023, **37**(12), 2350114.
9 G. A. Kumar and Shivashankar, *Int. J. Energy Environ. Eng.*, 2022, **13**(1), 77–103.
10 M. Mehrabian, M. Taleb-Abbasi and O. Akhavan, *Environ. Sci. Pollut. Res.*, 2023, **30**(56), 118754–118763.
11 S. Chala, N. Sengouga, F. Yakuphanoğlu, S. Rahmane, M. Bdirina and İ. Karteri, *Energy*, 2018, **164**, 871–880.
12 C. R. Almeyda, C. L. R. Rincón, A. S. Sepúlveda, M. A. Botero and M. A. Mantilla, *Ing. Compet.*, 2024, **26**(3), e20113982.
13 P. Panda, S. Beriha and S. K. Tripathy, *Optik*, 2024, **296**, 171550.
14 G. Wang, J. Chang, J. Bi, M. Lei, C. Wang and Q. Qiao, *Sol. RRL*, 2022, **6**(4), 2100841.
15 A. Kumar, S. Singh, M. K. Mohammed and A. E. Shalan, *Sol. Energy*, 2021, **223**, 193–201.
16 Y. Li, S. Yang, S. Yan, X. Liu, G. Shi and T. He, *Adv. Funct. Mater.*, 2025, **35**(7), 2415331.
17 J. Qi, Z. Song, X. Zhao, J. Xu, H. Li, H. Wang, K. Liu, C. Sun, S. Yang, M. Yuan and T. He, *Adv. Funct. Mater.*, 2025, 2425490.
18 S. Ijaz, E. Raza, Z. Ahmad, M. Zubair, M. Q. Mehmood, H. Mehmood, Y. Massoud and M. M. Rehman, *Sol. Energy*, 2023, **250**, 108–118.
19 X. Li, G. Shen, X. R. Ng, Z. Liu, Y. Meng, Y. Zhang, C. Mu, Z. G. Yu and F. Lin, *Energy Environ. Mater.*, 2023, **6**(5), e12439.
20 A. Rahmoune and O. Babahani, *J. Opt.*, 2024, 1–21.
21 H. Abnavi, D. K. Maram and A. Abnavi, *Opt. Mater.*, 2021, **118**, 111258.
22 A. Rahmoune and O. Babahani, *Optik*, 2023, **283**, 170875.
23 P. Sahoo, C. Tiwari, S. Kukreti and A. Dixit, *J. Alloys Compd.*, 2024, **981**, 173599.
24 K. Kumari, T. Chakrabarti, A. Jana, D. Bhattachartjee, B. Gupta and S. K. Sarkar, *Opt. Mater.*, 2018, **84**, 681–688.
25 M. A. Tamerd, B. Abraime, A. Kadiri, A. Lahmar, M. El Marssi, M. Hamedoun, A. Benyoussef and A. El Kenz, *J. Magn. Magn. Mater.*, 2021, **539**, 168402.
26 M. U. Salman, M. Bilal, Y. K. Karmani, U. Ali, S. M. Ramay, M. Younis and S. Atiq, *J. Mater. Chem. A*, 2025, **13**(20), 15057–15066.
27 A. N. Abena, A. T. Ngoupo, F. A. Abega and J. M. B. Ndjaka, *Chin. J. Phys.*, 2022, **76**, 94–109.
28 J. Chang, L. Jiang, G. Wang, W. Zhao, Y. Huang and H. Chen, *Phys. Chem. Chem. Phys.*, 2021, **23**(26), 14449–14456.
29 T. O. Ahmed, T. T. Ibrahim, E. O. Oladimeji and J. D. Koffa, *Braz. J. Phys.*, 2024, **54**(2), 42.
30 H. Arbouz, *J. Eng. Res.*, 2024, **12**(4), 610–615.
31 M. Pitaro, E. K. Tekelenburg, S. Shao and M. A. Loi, *Adv. Mater.*, 2022, **34**(1), 2105844.
32 C. Karuppaiah, D. Azhakanantham, M. Selvamani, T. D. Dongale, M. A. Alotaibi and A. V. Kesavan, *J. Mater. Sci.: Mater. Electron.*, 2024, **35**(30), 1936.
33 M. Kumar, S. K. Pundir and D. V. Singh, *Mater. Today Commun.*, 2024, **38**, 107841.
34 M. Ameen, M. Bilal, M. U. Salman, M. Luqman, S. M. Ramay, W. Mahmood and S. Atiq, *RSC Adv.*, 2025, **15**(32), 25799–25810.
35 A. S. Koigerov and A. V. Korlyakov, *Russ. Microelectron.*, 2022, **51**(4), 226–235.
36 G. Pindolia, S. M. Shinde and P. K. Jha, *Sol. Energy*, 2022, **236**, 802–821.
37 M. Minbashi and E. Yazdani, *Sci. Rep.*, 2022, **12**(1), 14916.
38 M. A. Nalianya, C. Awino, H. Barasa, V. Odari, F. Gaitho, B. Omogo and M. Mageto, *Optik*, 2021, **248**, 168060.
39 U. M. Umama, M. I. E. Jalal, M. A. F. Siddique, U. Chowdhury, M. I. U. Hoque and M. J. Rahman, *J. Phys. Chem. Solids*, 2025, **198**, 112480.
40 R. K. Yadav, P. S. Pawar, R. Nandi, K. E. Neerugatti, Y. T. Kim, J. Y. Cho and J. Heo, *Sol. Energy Mater. Sol. Cells*, 2022, **244**, 111835.
41 S. Sarker, M. T. Islam, A. Rauf, H. Al Jame, M. R. Jani, S. Ahsan, M. S. Islam, S. S. Nishat, K. M. Shorowordi and S. Ahmed, *Sol. Energy*, 2021, **225**, 471–485.
42 Y. K. Karmani, M. Bilal, M. U. Salman, M. Ameen, M. Luqman, S. M. Ramay, M. Younis and S. Atiq, *Mater. Sci. Eng., B*, 2025, **321**, 118484.
43 H. Ahmadi, M. Shahrostami and N. Manavizadeh, *Alex. Eng. J.*, 2024, **94**, 80–89.
44 Y. Li, X. Zhao, N. Meng, S. Dong, S. Yan, M. Yang and T. He, *Adv. Mater.*, 2025, e05694.
45 X. Li, Y. Li, Y. Feng, J. Qi, J. Shen, G. Shi, S. Yang, M. Yuan and T. He, *Adv. Mater.*, 2024, **36**(23), 2401103.
46 K. W. Lee, W. Lim, M. S. Jeon, H. Jang, J. Hwang, C. H. Lee and D. R. Kim, *Adv. Funct. Mater.*, 2022, **32**(1), 2105882.

47 M. S. Salem, A. Shaker, A. Zekry, M. Abouelatta, A. Alanazi, M. T. Alshammari and C. Gontand, *Energies*, 2021, **14**(18), 5741.

48 M. K. Hossain, G. I. Toki, A. Kuddus, M. K. Mohammed, R. Pandey, J. Madan, S. Bhattarai, M. F. Rahman, D. K. Dwivedi, M. Amami, H. Bencherif and D. P. Samajdar, *Mater. Chem. Phys.*, 2023, **308**, 128281.

49 M. K. Hossain, A. A. Arnab, R. C. Das, K. M. Hossain, M. H. K. Rubel, M. F. Rahman, H. Bencherif, M. E. Emetere, M. K. Mohammed and R. Pandey, *RSC Adv.*, 2022, **12**(54), 35002–35025.

50 G. A. Nowsherwan, A. Samad, M. A. Iqbal, T. Mushtaq, A. Hussain, M. Malik, S. Haider, P. V. Pham and J. R. Choi, *Nanomaterials*, 2022, **12**(10), 1767.

51 S. Valizadeh, A. Shokri, A. Sabouri-Dodaran, N. Fough and F. Muhammad-Sukki, *Results Phys.*, 2024, **57**, 107351.

52 A. Raj, M. Kumar, A. Kumar, K. Singh, S. Sharma, R. C. Singh, M. S. Pawar, M. Z. A. Yahya and A. Anshul, *Ceram. Int.*, 2023, **49**(1), 1317–1327.

53 M. Aliaghayee, *J. Electron. Mater.*, 2023, **52**(4), 2475–2491.

54 M. K. Hossain, M. A. Islam, M. S. Uddin, P. Paramasivam, J. A. Hamid, R. A. Alshgari, V. K. Mishra and R. Haldhar, *Sci. Rep.*, 2024, **14**(1), 1–22.

55 D. Parajuli, D. Kc, K. B. Khattri, D. R. Adhikari, R. A. Gaib and D. K. Shah, *Sci. Rep.*, 2023, **13**(1), 12193.

56 K. Kumar and P. Giri, *Opt. Quant. Electron.*, 2023, **55**(8), 690.

57 A. Bag, R. Radhakrishnan, R. Nekovei and R. Jeyakumar, *Sol. Energy*, 2020, **196**, 177–182.

58 M. Q. Kareem, S. S. Alimardan, W. M. Mohammad and I. M. Khudhair, *Results Surf. Interfaces*, 2025, **18**, 100411.

59 M. U. Salman, M. Mehak, U. Ali, G. M. U. Din, S. M. Ramay, M. Younis and S. Atiq, *RSC Adv.*, 2025, **15**(20), 15618–15629.

60 S. T. Jan and M. Noman, *Sol. Energy*, 2022, **237**, 29–43.

61 M. Mottakin, D. K. Sarkar, V. Selvanathan, M. J. Rashid, K. Sobayel, A. M. Hasan, M. A. Islam, G. Muhammad, M. Shahiduzzaman and M. Akhtaruzzaman, *Optik*, 2023, **272**, 170232.

62 R. Malani, T. Pansuriya and V. Kheraj, *Opt. Mater.*, 2022, **133**, 112910.

63 B. K. Ravidas, A. R. Kumar, A. Praveen, S. K. Agnihotri, S. Bhattarai, R. Pandey, J. Madan, S. Singh, M. K. Hossain, M. K. Roy and D. P. Samajdar, *J. Phys. Chem. Solids*, 2025, **196**, 112325.

64 B. Dahal, M. D. Rezaee, R. C. Gotame and W. Li, *Mater. Today Commun.*, 2023, **36**, 106846.

65 M. T. Islam and M. Sk, *Opt. Quant. Electron.*, 2025, **57**(4), 1–27.